The Astrophysical Journal, 891:139 (13pp), 2020 March 10 https://doi.org/10.3847/1538-4357/ab74d3

Mass Bias of Weak-lensing Shear-selected Galaxy Cluster Samples

Kai-Feng Chen[1,2,3], Masamune Oguri[4,5,6], Yen-Ting Lin[3], and Satoshi Miyazaki[7,8]
[1] Department of Physics, National Taiwan University, Taiwan; kfchen@asiaa.sinica.edu.tw
[2] Department of Mathematics, National Taiwan University, Taiwan
[3] Institute of Astronomy and Astrophysics Academia Sinica, Taipei 10617, Taiwan; b04901029@ntu.edu.tw
[4] Research Center for the Early Universe, University of Tokyo, Tokyo 113-0033, Japan
[5] Department of Physics, University of Tokyo, Tokyo 113-0033, Japan
[6] Kavli Institute for the Physics and Mathematics of the Universe (Kavli IPMU, WPI), University of Tokyo, Chiba 277-8582, Japan
[7] National Astronomical Observatory of Japan, 2-21-1 Osawa, Mitaka, Tokyo 181-8588, Japan
[8] Department of Astronomical Science, The Graduate University for Advanced Studies (Sokendai), 2-21-1, Osawa, Mitaka, Tokyo 181-8588, Japan
Received 2019 November 26; revised 2020 February 6; accepted 2020 February 9; published 2020 March 13

Abstract

We estimate the Eddington bias on weak-lensing mass measurements of shear-selected galaxy cluster samples. The mass bias is expected to be significant because constructions of cluster samples from peaks in weak-lensing mass maps and measurements of cluster masses from their tangential shear profiles share the same noise. We quantify this mass bias from large sets of mock cluster samples with analytical density profiles and realistic large-scale structure noise from ray-tracing simulations. We find that, even for peaks with signal-to-noise ratio larger than 4.0 in weak-lensing mass maps constructed in a deep survey with a high source galaxy number density of 30 arcmin^{-2}, derived weak-lensing masses for these shear-selected clusters are still biased high by ∼55% on average. Such a large bias mainly originates from upscattered low-mass objects, which is an inevitable consequence of selecting clusters with a noisy observable directly linked to the mass measurement. We also investigate the dependence of the mass bias on different physical and observational parameters, finding that the mass bias strongly correlates with cluster redshifts, true halo masses, and selection signal-to-noise thresholds, but having moderate dependence on observed weak-lensing masses and survey depths. This bias, albeit considerable, can still be modeled accurately in statistical studies of shear-selected clusters, as the intrinsic scatter around the mean bias is found to be reasonable in size. We demonstrate that such a bias can explain the deviation in X-ray properties previously found on a shear-selected cluster sample. Our result will be useful for turning large samples of shear-selected clusters available in future surveys into potential probes of cosmology and cluster astrophysics.

Unified Astronomy Thesaurus concepts: Observational cosmology (1146); Galaxy clusters (584); Weak gravitational lensing (1797)

1. Introduction

Clusters of galaxies have proven to be a sensitive probe of cosmology (for a review, see Allen et al. 2011). The number counts of these gravitationally collapsed structures are, in particular, sensitive to both the geometry and the structure formation history in our universe. The availability of clusters across a large redshift range allows us to obtain better constraints on dynamic parameters such as the dark energy equation of state compared to analyses relying on a single snapshot of the cosmic history (Weinberg et al. 2013). Modern cluster cosmology constraints are usually derived from complex likelihood analyses (Vikhlinin et al. 2009; Mantz et al. 2010, 2014; Rozo et al. 2010; de Haan et al. 2016; Planck Collaboration et al. 2016; Bocquet et al. 2019), whose success relies heavily on one's ability to understand the relations between halo masses and various observables from which cluster samples are selected.

Large cluster samples suitable for constraining cosmology are usually selected through observables that are related to baryonic properties of galaxy clusters. Indeed, due to the extreme environment within these massive systems, the swarming galaxies and the hot intracluster medium (ICM) can be detected across a wide range of wavelengths. Modern cluster samples are usually constructed through observations in one of the following three wavelength regimes: with X-ray signals (e.g., Edge et al. 1990; Gioia et al. 1990; Vikhlinin et al. 1998; Clerc et al. 2014) from the thermal bremsstrahlung, at millimeter wavelengths (e.g., Hasselfield et al. 2013; Bleem et al. 2015; Planck Collaboration et al. 2016) as a result of the thermal Sunyaev–Zel'dovich effect (Sunyaev & Zeldovich 1972), and in the optical via overdensities of red galaxies (e.g., Gladders & Yee 2005; Koester et al. 2007; Oguri 2014; Rykoff et al. 2016) or probing clustering directly with the matched filter technique (e.g., Wen et al. 2009; Milkeraitis et al. 2010; Szabo et al. 2011; Bellagamba et al. 2018). These observables are linked to halo masses through semiempirical scaling relations. Using these baryonic properties alone to constrain free parameters in the scaling relations together with the cosmological parameters, a framework known as *self-calibration* (Majumdar & Mohr 2004), is usually difficult. State-of-the-art cluster cosmology analyses require additional mass information to perform *mass calibration* on these samples (e.g., Wu et al. 2010; Oguri & Takada 2011; Huterer et al. 2015).

Weak gravitational lensing is one of the best means to provide an accurate mass estimate (e.g., Bardeau et al. 2007; Hoekstra 2007; Hamana et al. 2009; Okabe et al. 2010; Zhang et al. 2010; Mahdavi et al. 2013; Okabe & Smith 2016; Umetsu et al. 2016; Dietrich et al. 2019). Measurements of shape distortions of background galaxies, a quantity often referred to as the shear, can be used to derive nearly unbiased projected cluster masses on average (Clowe et al. 2004; Corless & King 2007; Becker & Kravtsov 2011; Bahé et al. 2012). However, cluster masses derived from weak lensing suffer from various sources of scatter and are often of low signal-to-noise ratio (S/N). Thus, a large

number of clusters with weak-lensing mass measurements are still needed to reduce the uncertainties in the mass–observable relations to provide accurate cosmological constraints.

On the other hand, recent wide and deep optical surveys offer an opportunity to construct cluster samples in an alternative way, that is, through identifying peaks in mass maps reconstructed from weak-lensing shear maps (e.g., Wittman et al. 2001; Miyazaki et al. 2007, 2015, 2018; Schirmer et al. 2007; Shan et al. 2012). Using these shear-selected samples is advantageous for cosmological studies, as they follow a more direct mass–observable relation and their selection functions can be quantified accurately using analytical calculations and ray-tracing simulations (Hamana et al. 2012; Miyazaki et al. 2018).

The sample of such shear-selected clusters is also useful for understanding the mass–observable relations better, given that they represent a sample of clusters selected solely through their mass distributions and their selection functions are therefore not directly affected by complex baryon physics. For instance, Giles et al. (2015) studied X-ray properties of shear-selected clusters from Miyazaki et al. (2007) to find that shear-selected clusters appeared to be X-ray underluminous for a given mass by a factor of ∼2–3 compared with X-ray-selected clusters. A recent paper by Miyazaki et al. (2018), who constructed a large homogeneous sample of shear-selected clusters from the Subaru Hyper Suprime-Cam (HSC) survey (Aihara et al. 2018), reached a similar conclusion based on analyses of archival X-ray data and comparisons with published X-ray catalogs. However, whether these clusters are really X-ray underluminous or their masses are overestimated needs to be examined more carefully first. We need to carefully quantify the selection effects of shear-selected clusters and study their impact on the X-ray luminosity–mass relation.

This work serves as a preparatory step for cluster studies utilizing shear-selected clusters by investigating their mass–observable relation under a fixed cosmology. Roughly speaking, we explore the distribution $P(\gamma|M, z)$, where γ denotes the observable, namely, the weak-lensing shear profile, and M and z represent the underlying halo mass and redshift. This distribution can be decomposed into $P(\gamma|M, z) = \int P(\gamma|M_{\rm obs}, z)P(M_{\rm obs}|M, z)\mathrm{d}M_{\rm obs}$, in which the dummy variable is taken to be the derived weak-lensing mass. When the cosmology is fixed, $P(\gamma|M_{\rm obs}, z)$ depends only on the halo profile one assumes to fit the shear profile. Thus, it suffices to study the distribution $P(M_{\rm obs}|M)$, which encapsulates the bias and uncertainty of the derived weak-lensing mass. The bias and uncertainties of cluster masses in weak-lensing analyses have already been thoroughly studied (Clowe et al. 2004; Oguri et al. 2005; Corless & King 2007; Meneghetti et al. 2010; Becker & Kravtsov 2011; Oguri & Hamana 2011; Bahé et al. 2012). These results of the mass bias and scatter are often quoted directly in cluster cosmology studies or measurements of cluster scaling relations, albeit without considering the impact of selection effects. Such an omission may be justified, as previous studies are mostly based on clusters selected through baryonic properties for which the correlation between scattering in baryonic properties and halo masses is of higher orders. In the context of shear-selected clusters, however, such a correlation is direct and might potentially lead to large bias if we derive $M_{\rm obs}$ from weak-lensing shear profiles, as is commonly done in the literature, because the selection of peaks in mass maps and the calculation of $M_{\rm obs}$ share the same noise, leading to significant distortions of $P(M_{\rm obs}|M)$. Such a bias is commonly referred to as the Eddington bias (Eddington 1913), and it is precisely the goal of this paper to characterize this well-known bias in the context of weak-lensing surveys.

This paper is organized as follows. In Section 2, we introduce the forward modeling framework and analyses we adopt in order to resemble the mass bias in real observations. Results and discussions are presented in Section 3. As an immediate application, we discuss in Section 4 the possibility of resolving the anomalous X-ray property found in shear-selected clusters (Giles et al. 2015) using our results. Conclusions are given in Section 5.

2. Methodology

To investigate bias of weak-lensing masses for shear-selected clusters, we create mock halo catalogs and generate observed weak-lensing mass maps assuming various survey depths to simulate this issue in existing and future surveys.

In Section 2.1, we introduce the basic framework in which we calculate the weak-lensing mass maps. Since the final samples are obtained through high-S/N cuts that inevitably limit the sample size, in order to achieve high statistical significance, we adopt a hybrid framework, in which the analytical halo model is combined with the uncorrelated large-scale structure (LSS) noise from ray-tracing simulations, rather than fully resorting to numerical simulations. This hybrid approach allows us to simulate a large number of halos in a reasonably short timescale. Around each simulated halo, the weak-lensing mass map is simulated by adding the uncorrelated LSS noise and the statistical noise to assign an S/N value to each simulated halo. Multiple samples are obtained through adjusting the survey depths to generate the mass map and the S/N cuts.

The treatments presented in Section 2.1 are mostly based on calculation from first principles. In Section 2.2, we discuss the uncertainties originating from the triaxial nature of halos. Since such uncertainties are more complex to model from first principles, we rely on statistical relations obtained in previous studies to take them into account. Lastly, in Section 2.3, we derive masses for clusters in each of these samples through a maximum likelihood estimation. The results are presented in Section 3.

2.1. The Mock Cluster Samples

The mock samples are set up in the following eight steps, which we describe in turn:

1. We adopt the 9 yr *Wilkinson Microwave Anisotropy Probe* cosmological parameters (Hinshaw et al. 2013)[9] as our input cosmology and consider a mock survey with an area of 5000 deg^2. The mock halo sample is then generated as a Poisson realization of the halo mass function (Tinker et al. 2008). In our calculations, we consider cluster samples with $M_{200c} \geqslant 10^{13}\ h^{-1}\ M_{\odot}$, where $M_{\Delta c}$ stands for the mass enclosed within the radius $r_{\Delta c}$, where the average density inside is Δ times the critical density of the universe. The redshifts of our samples range from $z = 0.01$ to 1.51, roughly corresponding to the range where optical cluster-finding algorithms are able to probe. For our particular experiment, we have created 778,651 halos in this step.

[9] More specifically, we adopt the parameters given in the column "+eCMB+BAO+H_0" of Table 4 in Hinshaw et al. (2013).

2. For each halo with mass $M = M_{200c}$ and redshift $z = z_{cl}$ in our mock catalog, we assign to it a concentration $c = c_{200c}$ from the distribution

$$P(c|M, z) = \frac{1}{\sqrt{2\pi}\,\sigma_{\ln c}}\frac{1}{c}\exp\left[-\frac{[\ln c - \ln \bar{c}(M, z)]^2}{2\sigma^2_{\ln c}}\right], \quad (1)$$

where the function $\bar{c}(M, z)$ is taken from the mass–concentration relation in Diemer & Joyce (2019) and we adopt $\sigma_{\ln c} = 0.25$, which is adequate for the redshift and mass range considered here (B. Diemer 2020, private communication).

3. In this step, we compute the tangential shear profile on the sky that is due solely to the halo itself, denoted as $\gamma_{\rm NFW}(\theta)$, by assuming that the density profile of dark matter halos follows the Navarro et al. (1997, hereafter NFW) profile

$$\rho_{\rm NFW}(r) = \frac{\rho_s}{(r/r_s)(1 + r/r_s)^2}, \quad (2)$$

where parameters ρ_s and r_s are computed as

$$\rho_s = \frac{200\rho_{\rm cri}(z_{cl})}{3}\frac{c^3}{\ln(1 + c) - c/(1 + c)}; \quad r_s = \frac{r_{200c}}{c}, \quad (3)$$

with $\rho_{\rm cri}(z_{cl})$ being the critical density of the universe at that redshift. It is then straightforward to compute $\gamma_{\rm NFW}(\theta)$ as

$$\gamma_{\rm NFW}\left(\theta := \frac{r_{\rm proj}}{D_A(z_{cl})}\right) = \frac{\Delta\Sigma(\theta)}{\Sigma_{\rm cri}} := \frac{\bar{\Sigma}(<\theta) - \Sigma(\theta)}{\Sigma_{\rm cri}}, \quad (4)$$

where

$$\Sigma(\theta) := \int {\rm d}x_3\, \rho_{\rm NFW}\left(\sqrt{x_3^2 + r_{\rm proj}^2}\right). \quad (5)$$

For these calculations, we use the analytic expressions found in Wright & Brainerd (2000). The reciprocal critical surface density is calculated as

$$\Sigma^{-1}_{\rm cri}(z_{cl}, z_s) = \begin{cases} 0 & \text{if } z_s \leqslant z_{cl}, \\ \dfrac{4\pi G}{c^2}\dfrac{D(z_{cl})D(z_{cl}, z_s)}{D(z_s)} & \text{otherwise}, \end{cases} \quad (6)$$

where $D(z_{cl})$ and $D(z_s)$ are angular diameter distances between the lens and the observer and between the source and the observer, respectively, whereas $D(z_{cl}, z_s)$ is the angular diameter distance between the source and the lens. In reality, since source galaxies are distributed across a wide range of redshifts, one should consider the ensemble average of $\Sigma^{-1}_{\rm cri}(z_{cl}, z_s)$. The distribution of source galaxies varies from survey to survey. In order to investigate the impact of the mass bias in different surveys, we set up a one-parameter fiducial model for the distribution, $P_{\rm gal}(z_s)$, as a function of the number density of source galaxies $n_{\rm gal}$ following Van Waerbeke et al. (2001),

$$P_{\rm gal}(z_s) \propto z_s^2 \exp\left(-\frac{z_s}{z_0}\right); \quad z_0 = \frac{1}{3}\left(\frac{n_{\rm gal}}{30}\right)^{1/3}. \quad (7)$$

In this paper, we set up experiments for $n_{\rm gal} = 10$, 20, 25, 30, 40, and 100 arcmin^{-2} to simulate various past and future surveys. Figure 1 shows $P_{\rm gal}(z_s)$ for these values of $n_{\rm gal}$ used in this paper. This profile can approximate the source redshift distribution of real galaxies in, e.g., the Subaru HSC survey (Aihara et al. 2018) well. The ensemble average of $\Sigma^{-1}_{\rm cri}(z_{cl}, z_s)$ is then given by

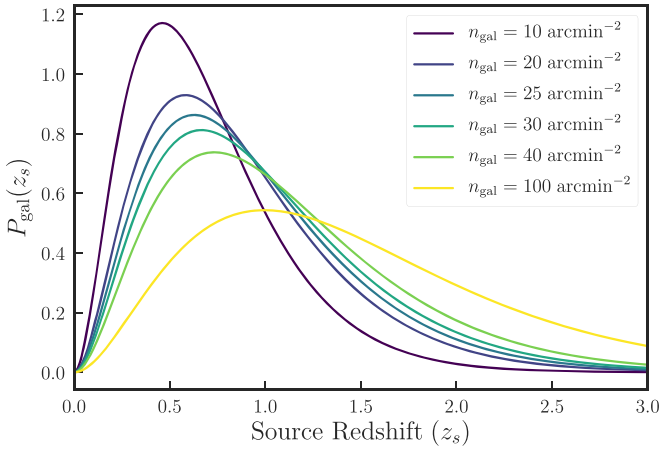

Figure 1. Fiducial models (Equation (7)) of the probability density function for source galaxies as a function of redshift with source galaxy number densities $n_{\rm gal} = 10$, 20, 25, 30, 40, and 100 arcmin^{-2} adopted in this paper.

$$\langle\Sigma^{-1}_{\rm cri}\rangle(z_{cl}) = \int_0^\infty \Sigma^{-1}_{\rm cri}(z_{cl}, z_s)P_{\rm gal}(z_s){\rm d}z_s. \quad (8)$$

We caution that the source redshift range of the above integral should be chosen carefully depending on the setup of the analysis. In weak-lensing analysis, one often selects source galaxies behind the lens, as the foreground galaxies add only noise but not signal. However, as we are using this shear profile to generate a mass map and select clusters from this map, at the point of calculating the mass map, we have no prior knowledge of the redshift of our potential candidates. Thus, all the quantities needed to construct the mock mass map have to be integrated over the whole line of sight. This subtlety needs to be dealt with carefully later when adding the random statistical noise (see step 6 below).

4. The mass map is obtained by convolving the shear map with a filter that maximizes the convergence signal from massive galaxy clusters and suppresses the average LSS contribution. Following Miyazaki et al. (2018), we choose a truncated and compensative Gaussian filter (Hamana et al. 2012)

$$U_G(\theta) = \begin{cases} \dfrac{1}{\pi\theta_s^2}\exp\left(-\dfrac{\theta^2}{\theta_s^2}\right) - U_0 & \text{if } \theta \leqslant \theta_{\rm out}, \\ 0 & \text{otherwise}, \end{cases} \quad (9)$$

and the respective filter for the tangential shear profile is

$$Q_G(\theta) = \frac{2}{\theta^2}\left(\int_0^\theta U_G(\tilde{\theta})\,\tilde{\theta}\,{\rm d}\tilde{\theta}\right) - U_G(\theta)$$
$$= \begin{cases} \dfrac{1}{\pi\theta^2}\left[1 - \left(1 + \dfrac{\theta^2}{\theta_s^2}\right)\exp\left(-\dfrac{\theta^2}{\theta_s^2}\right)\right] & \text{if } \theta \leqslant \theta_{\rm out}, \\ 0 & \text{otherwise}. \end{cases} \quad (10)$$

Following Miyazaki et al. (2018), we choose the smoothing radius $\theta_s = 0\ \!.'5$ and the truncation radius $\theta_{\rm out} = 15'$. The parameter U_0 in Equation (9) is introduced to let the filter U_G be of average zero. We plot these filters in Figure 2.

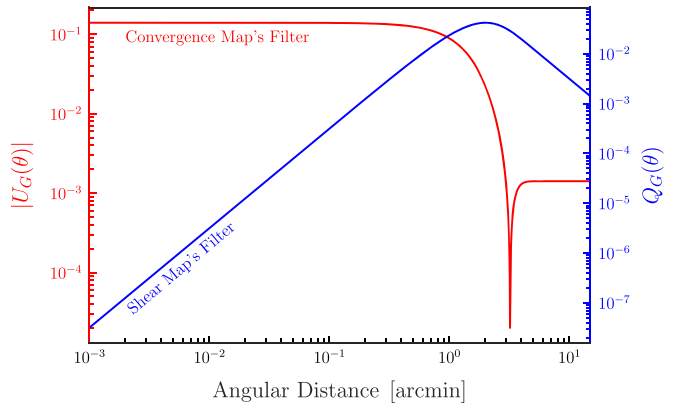

Figure 2. Truncated and compensative Gaussian filter we adopt in this paper. The filter for the convergence (Equation (9)) is shown in red, and the corresponding filter for the tangential shear profile (Equation (10)) is shown in blue.

In actual weak-lensing observations, the observable for a galaxy cluster is the reduced shear profile $g(\theta)$ derived from the average ellipticity of background source galaxies. Here we adopt the approximation that $g(\theta) \approx \gamma(\theta)$ for all $\theta \leqslant \theta_{\rm out}$. This approximation generally does not hold at small radius, as the convergence signal is large in the central region of the halo. However, as the reduced shear profile will be convolved with the filter $Q_G(\theta)$ that down-weights the signal from the center as shown in Figure 2, our approximation is justified. Thus, the NFW signal $\mathcal{S}_{\rm NFW}$ assigned to each cluster is

$$\mathcal{S}_{\rm NFW} = 2\pi \int_0^\infty \gamma_{\rm NFW}(\theta) Q_G(\theta)\, \theta {\rm d}\theta. \tag{11}$$

5. The contamination from LSS along the line of sight is approximated to first order by randomly painting our mock halos onto numerical simulated density field. For this purpose, we utilize the ray-tracing simulations presented by Sato et al. (2009), because these ray-tracing simulations have a relatively high angular resolution with a pixel size of $\sim 0\farcm15$ and thus are suited for out study focusing on clusters of galaxies. In their work, they performed high-resolution N-body simulations and projected particles onto multiple lens planes. 1000 ray-tracing realizations were then constructed through randomly shifting the underlying density field. In each realization, light sources are placed at $z_s \approx 0.6$, 0.8, 1.0, 1.5, 2.0, and 3.0, resulting in an ensemble of six 5 deg $\times$ 5 deg weak-lensing maps to be weighted according to the chosen source redshift distribution. For each halo in our catalog, we randomly choose a realization with a random position on the map. The tangential shear profile contributed from the LSS, denoted as $\gamma_{\rm LSS}(\theta)$, is then calculated as the average tangential shear profile around that randomly chosen location and is weighted with the probability distribution $P_{\rm gal}(z_s)$ defined in Equation (7). In short,

$$\mathcal{S}_{\rm LSS} = \int_0^\infty \frac{\sum_{z_s \in S} \langle \gamma_{\rm LSS}^{z=z_s}(\theta)\rangle P_{\rm gal}(z_s)}{\sum_{z_s \in S} P_{\rm gal}(z_s)} Q_G(\theta) {\rm d}\theta, \tag{12}$$

where the angle bracket stands for the circular average in the two-dimensional weak-lensing shear map and S is the set of available source redshift slices.

6. Next, we estimate the statistical noise on the weak-lensing mass maps. Two major sources of errors in weak-lensing observations are the finiteness and the intrinsic ellipticity of source galaxies. We denote the variance of such an observational uncertainty as $\sigma^2_{\rm STAT}$. van Waerbeke (2000) has shown that such a variance can be quantified as

$$\sigma^2_{\rm STAT} = \frac{\sigma_\epsilon^2}{2n_{\rm gal}} \int_{-\infty}^{\infty} |W(\boldsymbol{k})|^2\, {\rm d}\boldsymbol{k}, \tag{13}$$

where σ_ϵ^2 is the variance characterizing the intrinsic ellipticity of source galaxies and the factor 2 accounts for the fact that the tangential shear is derived from one out of two components of galaxy ellipticities, $n_{\rm gal}$ is the surface number density of source galaxies, and $W(\boldsymbol{k})$ is the Fourier transform of the spatial filter one adopts to smooth the shear signal (Equation (10)). In this paper, we adopt $\sigma_\epsilon = 0.4$. By the Parseval–Plancherel identity and assuming the noise to be Gaussian, the noise due to observational uncertainty is thus

$$\mathcal{S}_{\rm STAT} \sim \mathcal{N}\left(0,\ \frac{\sigma_\epsilon^2}{2n_{\rm gal}} \int_0^\infty 2\pi |Q(\theta)|^2\, \theta {\rm d}\theta\right). \tag{14}$$

In practice, once we select clusters with a sufficiently large S/N, we will be able to obtain their redshift based on their optical counterparts. The shear profile will then be measured with background galaxies only, to increase the S/N. The noise in this shear profile measurement, combined with the noise due to foreground galaxies, is the source of the noise $\mathcal{S}_{\rm STAT}$ on the mass map. Thus, the two random noises cannot be generated independently. Therefore, instead of using Equation (14) directly, we first generate a random noise profile solely due to the background galaxies, which will be used later in step 8:

$$\gamma^{\rm bg}_{{\rm STAT},i} \sim \mathcal{N}\left(0,\ \frac{\sigma_\epsilon^2}{2N_{\rm bg,\,i}}\right), \tag{15}$$

$$N_{{\rm bg},i} = A_i n_{\rm gal} \int_{z_{cl}}^\infty P_{\rm gal}(z_s) {\rm d}z_s. \tag{16}$$

Here the index i runs over radial bins that are used in creating the tangential shear profile and A_i is the area of the ith bin. In this paper, we bin the shear profile from 0.2 to 7 h^{-1} Mpc into 20 bins to be consistent with the existing observational work of Miyazaki et al. (2018). As discussed in the end of step 3, $\mathcal{S}_{\rm STAT}$ should be due to noise across the whole line of sight. Thus, in addition to $\gamma^{\rm bg}_{\rm STAT}$, we also calculate the noise profile in the foreground

$$\gamma^{\rm fg}_{{\rm STAT},i} \sim \mathcal{N}\left(0,\ \frac{\sigma_\epsilon^2}{2N_{\rm fg,\,i}}\right), \tag{17}$$

$$N_{{\rm fg},i} = A_i n_{\rm gal} \int_0^{z_{cl}} P_{\rm gal}(z_s) {\rm d}z_s. \tag{18}$$

Combining the two noise profiles and convolving this with the desired filter, we obtain the final noise in the mass map

$$\gamma_{{\rm STAT},i} = \frac{N_{{\rm fg},i}\gamma^{\rm fg}_{{\rm STAT},i} + N_{{\rm bg},i}\gamma^{\rm bg}_{{\rm STAT},i}}{N_{{\rm fg},i} + N_{{\rm bg},i}}, \tag{19}$$

$$\mathcal{S}_{\rm STAT} = \sum_i (\gamma_{{\rm STAT},i} Q(\theta_i) A_i). \tag{20}$$

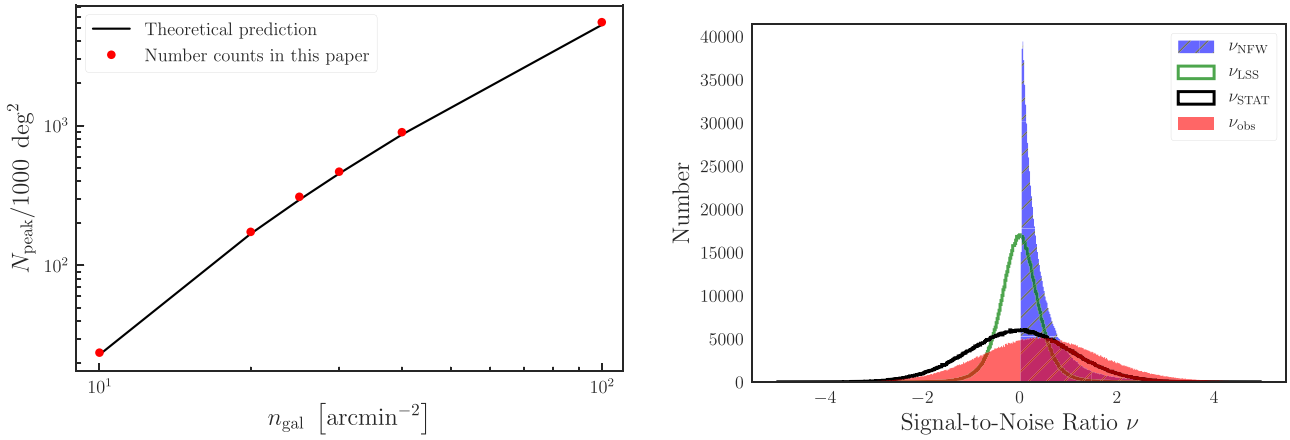

Figure 3. Left: comparison between number counts of shear peaks selected with a $\nu_{\rm threshold} = 4.7$ cut obtained in this paper and those calculated in Appendix A of Miyazaki et al. (2018). Right: distributions of ν for various components that are used to derive the final observed S/N of peaks, $\nu_{\rm obs}$, for a setup with $n_{\rm gal} = 30$ arcmin^{-2}.

One can easily check that $\mathcal{S}_{\rm STAT}$ generated as in Equation (20) follows the distribution of Equation (14) in the continuous limit.

7. We are now able to assign to each halo in our catalog an observable $\nu_{\rm obs}$ as

$$\nu_{\rm obs} = \frac{\mathcal{S}_{\rm NFW} + \mathcal{S}_{\rm LSS} + \mathcal{S}_{\rm STAT}}{\sigma_{\rm STAT}}, \tag{21}$$

which represents the S/N of a peak in the weak-lensing mass map for that halo. Equation (21) is normalized by $\sigma_{\rm STAT}$ because in observations the noise is estimated from many realizations of weak-lensing mass maps with randomly rotated source galaxies, which eliminates the LSS noise but retains only the statistical noise (see, e.g., Miyazaki et al. 2018). The shear-selected clusters are identified as those with $\nu_{\rm obs} \geqslant \nu_{\rm threshold}$. We vary the value of $\nu_{\rm threshold}$ to investigate the mass bias as a function of the selection criterion. Observationally, the redshift is given by their optical counterparts. Most of the state-of-the-art optical cluster-finding algorithms are able to produce a pure and complete cluster sample at low redshift and assign to them accurate photometric redshifts. For instance, the CAMIRA algorithm (Oguri 2014), adopted by the HSC Collaboration for generating the optical cluster catalogs, is able to estimate cluster (photometric) redshifts to high accuracy, $\sigma_z/(1+z) \lesssim 0.01$ for $z_{cl} \leqslant 0.8$ (Oguri et al. 2018). Furthermore, Miyazaki et al. (2018) have shown that peaks with high S/N, $\nu_{\rm obs} \geqslant 4.7$, found in HSC weak-lensing mass maps have optical counterparts almost completely. Thus, in this paper we assume that all peaks on the mass map are able to find optical counterparts and can be assigned with a z_{cl} with a negligible error.

8. For clusters selected in the above step, we also create mock tangential shear profiles that are used to derive weak-lensing masses for shear-selected clusters in Section 2.3. The main signal is the shear profile due to the massive halo itself as described in step 3. The only difference is that instead of using all the source galaxies along the line of sight to obtain the shear signal, we use only background galaxies as is often done in actual analyses. This setup alters the ensemble average of $\Sigma_{\rm cri}^{-1}(z_{cl}, z_s)$ from Equation (8) to

$$\langle \Sigma_{\rm cri}^{-1} \rangle (z_{cl}) = \frac{\int_{z_{cl}}^{\infty} \Sigma_{\rm cri}^{-1}(z_{cl}, z) P_{\rm gal}(z_s) {\rm d}z_s}{\int_{z_{cl}}^{\infty} P_{\rm gal}(z_s) {\rm d}z_s}. \tag{22}$$

This continuous signal $\gamma_{\rm NFW}^{\rm bg}(\theta)$ is binned into 20 bins in physical scale as discussed in step 6. Around the same location chosen in step 5, a shear profile due to the LSS is calculated using only background sources with $z_s \geqslant z_{cl}$. The statistical uncertainties only from background galaxies generated in Equation (15) are added to the profile. The resulting shear profile, $\gamma_{{\rm obs},i}^{\rm bg} = \gamma_{{\rm NFW},i}^{\rm bg} + \gamma_{{\rm LSS},i}^{\rm bg} + \gamma_{{\rm STAT},i}^{\rm bg}$ $(i = 1, \ldots, 20)$, is the mock observable that we use to derive the weak-lensing mass and quantify the mass bias.

To summarize, we fix a cosmology and change the input parameters $(n_{\rm gal}, \nu_{\rm threshold})$ to generate different shear-selected cluster samples with observables $(\nu_{\rm obs}, z_{cl}, \{\gamma_{{\rm obs},i}^{\rm bg}\}_{i=1,\ldots,20})$ that are to be analyzed in Section 2.3. Figure 3 shows some statistics for the catalog we created. The left panel shows the number of clusters that are selected with $\nu_{\rm threshold} = 4.7$ as a function of input $n_{\rm gal}$ in comparison with the analytic calculation performed in Appendix A of Miyazaki et al. (2018). The sample sizes increase substantially for deeper surveys, demonstrating the advantages of shear-selected cluster samples in the future. On the right panel, we show the typical level of scattering in the mass map. Since the signals from the halos themselves are buried in the noise except for very massive clusters, a large number of low-mass objects can be upscattered into our selections. Thus, we can already expect to find a considerable bias in shear-selected samples.

Lastly, we comment on the possible impacts the specific choice of mass–concentration relation and halo density profile might have on our mock cluster samples. The mass–concentration relation has been heavily studied in the literature, and a number of functional forms, calibrated with cosmological simulations, have been proposed to describe this relation (e.g., Bullock et al. 2001; Macciò et al. 2008; Prada et al. 2012; Ludlow et al. 2016; Diemer & Joyce 2019). Here we have examined that the distribution of our observable ν is basically unaffected under different choices of mass–concentration relation, especially for low-mass halos. Since we expect the

bias to be coming from upscattered low-mass objects, we believe that the impact from the choice of mass–concentration relation will be negligible. Meanwhile, in this paper we work with the NFW model to forecast the weak-lensing observable owing to the simplicity of its lensing properties. However, recent high-resolution cosmological simulations have found that the halo density profiles are more accurately described by the functional form proposed by Einasto (1965), especially at inner radii of halos (Graham et al. 2006; Merritt et al. 2006; Gao et al. 2008; Navarro et al. 2010). We have examined that changing the model will only slightly vary the value of ν owing to the shape of the filter we adopt in this paper. Moreover, the two models nearly coincide with each other at the radius range 0.3–7 h^{-1} Mpc we considered when generating the shear profile for most of our halos. Thus, we do not expect the choice of halo density profile to affect our derived weak-lensing mass either. On the other hand, we note that deviations from the spherical symmetry assumption for both models might induce a nonnegligible effect on our results. This will be discussed in the following subsection.

2.2. Impact of the Halo Nonsphericity

In reality, dark matter halos are complex, and their density profiles deviate from the simple NFW model we assume in Section 2.1. One of the potentially important sources of systematic errors comes from the triaxial shape of real halos (Warren et al. 1992). It has been shown that a spherical symmetric NFW fit to a triaxial halo can lead to an error larger than 30% in mass in some cases (Oguri et al. 2005; Corless & King 2007; Meneghetti et al. 2010; Becker & Kravtsov 2011; Oguri & Hamana 2011; Bahé et al. 2012). It may therefore be necessary to take these uncertainties into account.

However, addressing the triaxial nature of the halo density profiles directly is nontrivial. Although analytic triaxial profiles are described, for instance, in Jing & Suto (2002), statistical properties such as the mass–concentration relation in these frameworks are less well known among the literature. In this paper, we make use of existing studies to characterize these uncertainties in a statistical manner. Given a realistic halo with a mass $M_{\rm True}$, let $M_{\rm NFW}$ be the mass in which the corresponding spherical NFW profile best describes the projected surface density of the realistic halo. Becker & Kravtsov (2011) and Bahé et al. (2012) have shown that the distribution $P(M_{\rm NFW}|M_{\rm True})$ is well characterized by a lognormal distribution. Therefore, we assume

$$M_{\rm NFW} = b_{\rm NFW} M_{\rm True} e^{\Delta_{\rm NFW}}, \tag{23}$$

where $\Delta_{\rm NFW} \sim \mathcal{N}(0, \sigma^2_{\rm NFW})$. Previous studies such as Becker & Kravtsov (2011) have also determined these parameters through numerical simulations. In these simulations, both halo triaxiality and the line-of-sight projection contributed to the value of ($b_{\rm NFW}$, $\sigma_{\rm NFW}$). As the line-of-sight contribution has already been taken into account in Section 2.1, we need to separate the two when choosing ($b_{\rm NFW}$, $\sigma_{\rm NFW}$). Becker & Kravtsov (2011) have shown that the value $b_{\rm NFW}$ is independent of the line-of-sight integration length and is close to unity. Meanwhile, regardless of the halo mass or redshift, $\sigma_{\rm NFW}$ approaches 0.18 when the line-of-sight contribution vanishes. This result is roughly consistent with estimates of $\sigma_{\rm NFW}$ utilizing analytic triaxial profiles presented in Oguri et al. (2005), Oguri & Blandford (2009), and Hamana et al. (2012). Therefore, in this paper we choose $b_{\rm NFW} = 1$ and $\sigma_{\rm NFW} = 0.18$, which approximately corresponded to a 20% scatter in mass.

Thus, instead of using the true mass $M_{\rm True}$ to model the density profile in Equations (1) and (3), for each halo we draw an $M_{\rm NFW}$ according to Equation (23) and repeat all the steps after step 2 in Section 2.1 to forecast the weak-lensing signals. In this way, the uncertainties due to the triaxial nature of halos are approximately included. The mass bias from this sample is discussed in Section 3.2.

2.3. Mass Estimation for Shear-selected Clusters

To estimate masses for shear-selected clusters, we perform a maximum likelihood analysis on the cluster shear profile obtained in Section 2.1 or Section 2.2. The free parameters in our analysis are the mass M_{200c} and the concentration c_{200c}. Here, we adopt a Gaussian likelihood on the observed shear profile $\gamma_{\rm obs}$,

$$\log \mathcal{L}(\{\gamma^{\rm bg}_{{\rm obs},i}\}|M_{200c}, c_{200c}) = -\frac{1}{2}\sum_{i,j=1}^{20} \Delta\gamma_i^t \boldsymbol{C}_{ij}^{-1} \Delta\gamma_j;$$
$$\Delta\gamma_i := \gamma^{\rm bg}_{{\rm obs},i} - \gamma_{{\rm NFW},i}(M_{200c}, c_{200c}), \tag{24}$$

where $\boldsymbol{C}$ is the covariance matrix and $\gamma_{\rm NFW,i}$ are the binned analytic shear profile as described in step 3 in Section 2.1. Here we drop a constant term proportional to $\det \boldsymbol{C}$, as the covariance matrix is a function of the cluster redshift only, which is fixed in our analysis. The components of the covariance matrix are given by

$$\boldsymbol{C}_{ij} = {\rm cov}(\gamma_i, \gamma_j) = \frac{\sigma_\epsilon^2}{2N_{{\rm bg},i}}\delta_{ij} + \boldsymbol{C}_{{\rm LSS},ij}, \tag{25}$$

where δ_{ij} denotes the Kronecker delta and the term $\boldsymbol{C}_{\rm LSS,ij}$ denotes the contribution coming from the uncorrelated LSS (Hoekstra 2003). Here we ignore $\boldsymbol{C}_{\rm LSS,ij}$ for computational simplicity as is sometimes adopted in real observations.

In practice, we sample the physical parameters in logarithmic space using the affine-invariant ensemble sampler (Goodman & Weare 2010) implemented in the `emcee` package (Foreman-Mackey et al. 2013). We assume a flat prior in logarithmic space: $13 \leqslant \log_{10}(M_{200c}\, h/M_\odot) \leqslant 16$; $0 \leqslant \log_{10} c_{200c} \leqslant \log_{10}(20)$. The best-fit parameters are extracted as the 50th percentile of the samples excluding the burn-in period, and the uncertainties we quote are the 16th and 84th percentiles. Figure 4 shows an example of the mock shear profile $\{\gamma_{\rm obs,i}\}$ that we assign to a typical cluster and the resulting fit.

3. Results

The important quantity that we study in this paper is the mass bias of weak-lensing masses $M_{\rm obs}$ derived by fitting tangential shear profiles (Section 2.3) for shear-selected clusters. We define the mass bias b as

$$b := \frac{M_{\rm obs}}{M_{\rm True}}. \tag{26}$$

In this section, we present the mass bias as a function of different variables by computing the median among the values from clusters within a small bin of the respective variable. The error bars we draw always represent the 16th and 84th percentiles. In order to distinguish the origin of the mass bias, in the following we first focus on results for the simplest setup

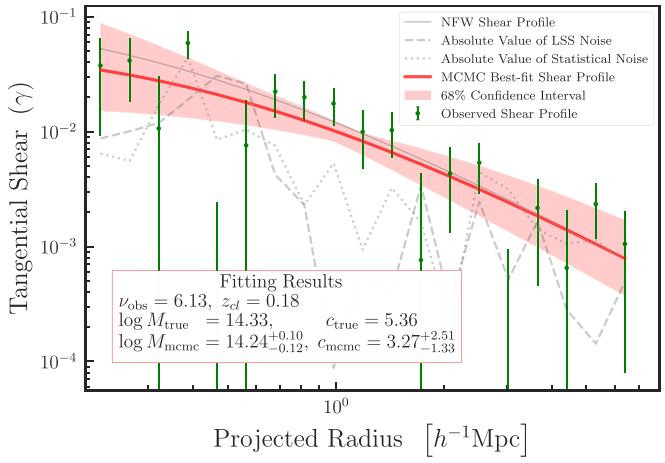

Figure 4. Example of mock tangential shear profile and the resulting fit. Contributions from individual components $\gamma^{\rm bg}_{{\rm NFW},i}$ (solid gray), $\gamma^{\rm bg}_{{\rm LSS},i}$ (dashed), and $\gamma^{\rm bg}_{{\rm STAT},i}$ (dotted) are shown for a typical cluster in our catalog with $n_{\rm gal} = 30\ {\rm arcmin}^{-2}$. The solid red line shows the best-fit shear profile with a 68% confidence interval for this particular case. The best-fit parameters are summarized in the inset.

in Section 2.1, i.e., samples without the effect of nonsphericity discussed in Section 2.3, to see the bias due solely to the selection, together with the statistical and LSS noises. The results with the inclusion of triaxiality will be presented in Section 3.2.

3.1. For Spherical Halos

To clearly see the effect of upscatter, for each shear-selected sample, we introduce a corresponding control sample for comparison. Suppose the given shear-selected sample is selected with $\nu_{\rm obs} \geqslant \nu_{\rm threshold}$; the control sample is then defined as those clusters with $\nu_{\rm NFW} \geqslant \nu_{\rm threshold}$. The control samples can be viewed as a truly mass-selected sample, and hence we expect them to be free from upscattered contaminants. The mass bias of these two samples will be shown in juxtaposition in the following.

Figure 5 shows the bias as a function of the input galaxies' number density $n_{\rm gal}$ under several different selection criteria $\nu_{\rm threshold}$. Here we clearly see that the bias of each control sample is approximately 1, while the observed samples are all biased high, demonstrating the existence of Eddington bias in shear-selected cluster samples. In Figure 5, the bias of the control sample is slightly below 1 owing to the nature of the noise profile. Although the control sample is selected with a noise-free observable, noise is still included in the shear profile when deriving the weak-lensing mass. Therefore, there will be some cases where noise dominates in the observed shear profile. Since the noise profile is flat, only a halo with very low concentration can accommodate such a profile. In these cases, the mass is determined by the average value of the profile, which will usually be lower than the value of the noise-free profile at inner radii owing to the steepness of the NFW profile, resulting in a lower best-fit weak-lensing mass. Such events will be rarer for larger $\nu_{\rm threshold}$ or $n_{\rm gal}$, and indeed, we find the bias to be closer to 1 in these samples as can be seen in Figure 5.

For the actual shear-selected samples, the dependencies of bias on $\nu_{\rm threshold}$ or $n_{\rm gal}$ are mainly affected by two factors. Under the same selection threshold, the lower $n_{\rm gal}$ samples are selecting clusters having larger $M_{\rm obs}$, as the noise level is higher in those samples, reducing the value of $\nu_{\rm obs}$ for a given cluster. Since the slope of the cluster mass function decreases as the mass increases, this leads to a larger fraction of upscattered objects in the lower-$n_{\rm gal}$ cases. Meanwhile, a higher noise level also allows for larger scattering. At higher $\nu_{\rm threshold}$, however, these effects become less significant. In reality, the shear-selected samples are usually selected with a high S/N threshold, e.g., $\nu_{\rm threshold} = 4.0$. Thus, in the following discussion we will focus on a specific case where $n_{\rm gal} = 30\ {\rm arcmin}^{-2}$, which roughly corresponds to the depth found in the Subaru HSC survey.

The relations between the bias and mass or redshift are of the greatest interest in our study, as these are often variables directly used in measuring cluster scaling relations. Understanding the bias as a function of these variables will help us correctly rectify the shape of scaling relations measured through shear-selected cluster samples.

The cluster mass affects the intrinsic strength of the weak-lensing shear signal. Lower-mass objects require a larger scatter in order to be selected in the sample, and as a result, the mass bias naturally increases as shown in the top panel of Figure 6. However, as the true mass is not a direct observable, we also show the mass bias as a function of the observed mass $M_{\rm obs}$. It is clear from the bottom panel of Figure 6 that there are two populations of clusters at a given $M_{\rm obs}$ range: those that have intrinsic mass in a similar mass range and those that are significantly upscattered. The situation of upscattering differs across $M_{\rm obs}$, but the overall bias seems to be constant within a reasonable range of $M_{\rm obs}$. We note that in the bottom panel of Figure 6 the apparent deviation of the mass bias for low-$M_{\rm obs}$ objects in the control sample is artificial. Unlike the shear-selected cluster samples, the selection on $\nu_{\rm NFW}$ will roughly correspond to a selection on mass, say, $M_{\rm True} \geqslant M_0$. Therefore, the bias $b = M_{\rm obs}/M_{\rm True}$ must be smaller than $M_{\rm obs}/M_0$. In particular, for $M_{\rm obs} < M_0$, the bias must be smaller than 1. For the particular control sample shown in Figure 6, 95% of the clusters have mass larger than $10^{14}\,h^{-1}\,M_\odot$. Taking this as M_0, this upper bound, which is shown in solid blue, clearly explains the trend we see in Figure 6.

The noise in the observed shear profile, on the other hand, is primarily sensitive to the redshift of the lens, as the number of source galaxies is more limited at higher redshift. This naturally causes the mass bias to increase as a function of redshift as can be seen in Figure 7. It is worth noting that in Figure 7 the control sample contains no cluster with $z \geqslant 0.9$, meaning that the cluster candidates observed in the shear-selected sample would not be selected if not for the large weak-lensing noise. Therefore, we are actually selecting a sample of purely upscattered clusters at higher redshift, and the bias naturally becomes high in these redshift bins.

For the above results, we show the mass bias in the sample selected with $\nu_{\rm threshold} \geqslant 4.0$. The mass bias as a function of this selection criterion is shown in Figure 8. In real observations, we often modify this lower limit to maximize the number of clusters in the final sample. However, as we lower the $\nu_{\rm threshold}$, we should also note that we are obtaining a more biased sample.

3.2. Inclusion of Triaxiality

It is now clear that the selection effect can cause a serious mass bias in a shear-selected cluster sample, even if we assume

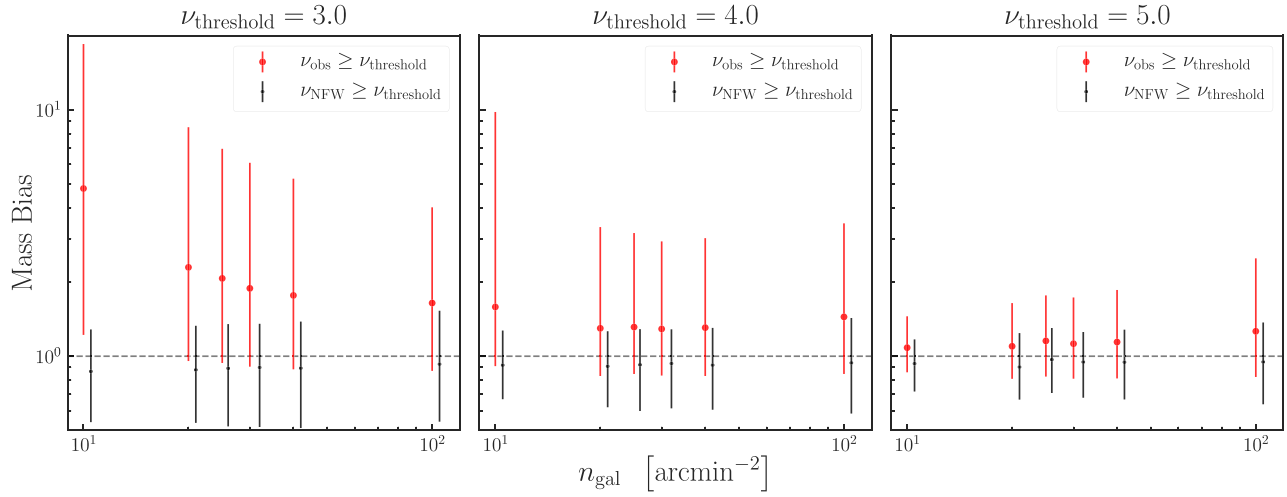

Figure 5. Mass bias (Equation (26)) as a function of galaxies' number density $n_{\rm gal}$ under three different selection criterion $\nu_{\rm threshold}$, $\nu_{\rm threshold} = 3.0$ (left), $\nu_{\rm threshold} = 4.0$ (middle), and $\nu_{\rm threshold} = 5.0$ (right). Large red circles show the results for the shear-selected samples, and small black circles show the results for the corresponding control samples that are selected based on noise-free $\nu_{\rm NFW}$ instead of $\nu_{\rm obs}$ to demonstrate that the bias is indeed caused by upscattering due to the noise. The positions of the control samples are slightly shifted rightward to avoid overlaps.

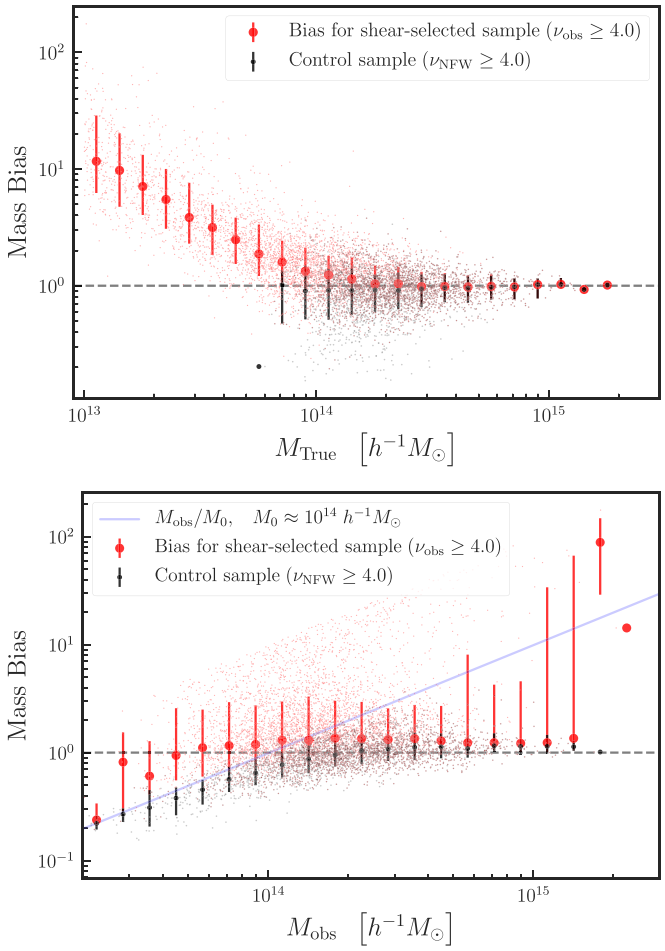

Figure 6. Mass bias (Equation (26)) as a function of true mass (top panel) and the observed weak-lensing mass (bottom panel). In both panels, large red circles correspond to the bias in the shear-selected cluster sample, whereas small black circles denote the bias in the corresponding control sample as in Figure 5. The solid blue line in the bottom panel shows the upper bound on the mass bias for the control sample.

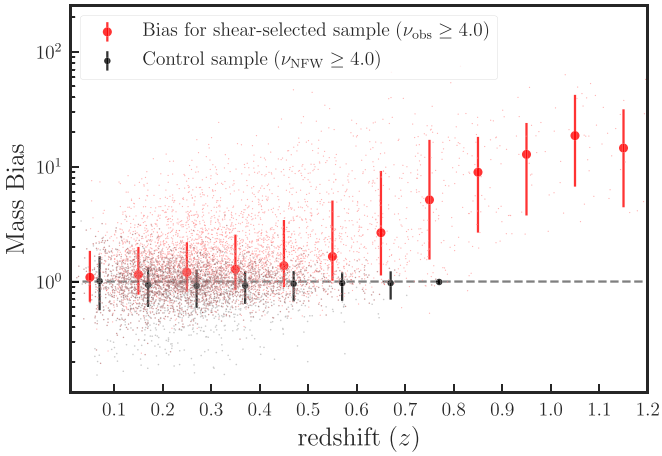

Figure 7. Mass bias (Equation (26)) as a function of the cluster redshift. Symbols are the same as in Figure 6. The redshift positions for the control sample are slightly shifted rightward to avoid overlaps.

a spherical halo as an input profile. Here we include additional scatter in mass due to halo triaxiality, which should make our estimate of the mass bias more realistic. We include the effect of halo triaxiality using the methodology described in Section 2.2. Similarly to the discussions above, we only focus on the fiducial case where $n_{\rm gal} = 30\,{\rm arcmin}^{-2}$.

An extra scatter in mass from triaxiality can contribute to our results in two ways: it can flatten out the mass function and can induce additional uncertainties in the tangential shear profile. The number density of clusters as a function of scattered mass is equal to the convolution of the original mass function with the distribution function of the induced scattering. Since we are considering a narrow lognormal scatter, the impact on the mass function is minor. For the mock cluster sample considered in this paper and a scatter of $\sigma_{\rm NFW} = 0.18$, the number of clusters in the low-mass end ($<10^{14}\,h^{-1}\,M_\odot$) is decreased by roughly 0.1%, and the number in the massive end ($>10^{14}\,h^{-1}\,M_\odot$) is increased by approximately 5%. As we are concerned with

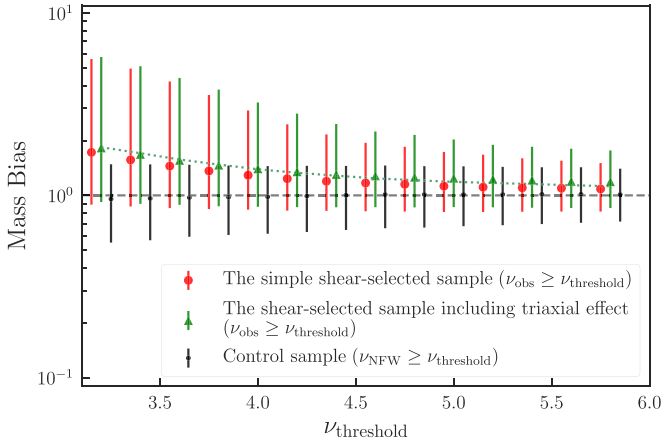

Figure 8. Mass bias (Equation (26)) as a function of the selection criterion $\nu_{\rm threshold}$. The large red circles show the sample constructed in Section 2.1, whereas the green triangles represent the sample including the modification of halo triaxiality from Section 2.2. The dotted green line shows a quantitative estimate of the results with halo triaxiality (see Section 3.2 for details). The large red circles and the small black circles are slightly shifted leftward and rightward, respectively, from the green triangles to avoid overlaps.

upscattering of low-mass objects, the portion of clusters that are upscattered can be treated the same as before given the same level of scattering. However, the level of scattering can increase owing to the extra uncertainty in the shear profile. Within a reasonable range of mass and redshift, a 20% increase in mass will result in a ∼10% increase in $\nu_{\rm NFW}$. The effect from such an additional uncertainty, however, is secondary compared to the large statistical noise.

Figure 8 shows the increase in the mass bias after we include the scatter due to triaxiality. Indeed, the increase in the mass bias is more significant at higher $\nu_{\rm threshold}$ selection as the triaxial scattering starts to become comparable to the statistical noise. Quantitatively, at a given $\nu_{\rm threshold} = \nu_0$, the level of statistical uncertainty is of order $\sim\nu_0^{-1}$. An additional 10% scatter in $\nu_{\rm obs}$ will raise the uncertainty to $\sim\sqrt{\nu_0^{-2} + 0.1^2}$. Equivalently, we can say that the additional scatter shifted the mass bias to the level where $\nu_{\rm threshold} = (\sqrt{\nu_0^{-2} + 0.1^2})^{-1}$. This estimate is plotted as the dotted green line in Figure 8. We find that our simple estimate matches the results on the mock sample quite well. For the fiducial case of $n_{\rm gal} = 30$ arcmin^{-2} and $\nu_{\rm threshold} = 4.0$, we find that the mass bias is ∼55% on average.

One of the main purposes of this paper is to serve as a preparatory step for cluster studies utilizing shear-selected cluster samples. So far we are concerned with the average mass bias, but when it comes to constraining scaling relations or cosmological parameters, the knowledge of the scatter in $P(M_{\rm obs}|M_{\rm True}, z_{cl})$ is also important. Even if the mass bias is larger in shear-selected cluster samples, tight constraints on cluster scaling relations or cosmological parameters are still possible if the distribution $P(M_{\rm obs}|M_{\rm True}, z_{cl})$ is not too dispersed. Figure 9 shows the probability density function (pdf) of the mass bias in a grid of $M_{\rm True}$ and z_{cl} for a sample selected with $\nu_{\rm obs} \geqslant 4.0$. We find that these distributions are well characterized by the lognormal distribution. In the upper left corner of each panel, we show the mean bias and the variance in $\ln b$. The corresponding lognormal pdf based on these parameters is overplotted. Although the mass bias is relatively large, the scatter of the distribution at each redshift and mass is comparable to those without a selection effect (Becker & Kravtsov 2011; Bahé et al. 2012). Therefore, using shear-selected samples in studies of scaling relations and cosmological parameters might indeed benefit from the absence of uncertainties in semiempirical mass–observable scaling relations without introducing additional scatter.

Finally, as a validation test, we demonstrate that the mass bias and scatter given in Figure 9, together with an analytical description of the selection function, can be used to recover the input halo mass function. Here we divide the cluster sample selected with $\nu_{\rm threshold} \geqslant 4.0$ into four redshift bins as in Figure 9 and count the number of clusters in 12 equally spaced mass bins from $\log_{10}(M_{200c}\, h/M_\odot) = 13$ to 15. The dotted histograms in Figure 10 show the observed halo mass function in different redshift bins. We can describe this observed mass function with the following integration:

$$\frac{{\rm d}N}{{\rm d}M_{\rm obs}{\rm d}z}(M_{\rm obs}, z|\nu_{\rm threshold}) = \int \left[P(M_{\rm obs}|M, z) \times \frac{{\rm d}N}{{\rm d}M{\rm d}z}(M, z) \times S(M, z|\nu_{\rm threshold}) \right] {\rm d}M, \quad (27)$$

where the selection function $S(M, z|\nu_{\rm threshold})$ is given in Equation (A9) of Miyazaki et al. (2018). In practice, we sample the number of clusters in each mass bin N_i $(i = 1, \ldots 12)$ with a flat prior between 0 and 50,000 while requiring the mass function to be strictly decreasing; we then scatter N_i according to the respective lognormal distribution given in Figure 9 and multiplied by the average value of the selection function in that bin. We use a Poisson likelihood to compare with the observed number count in each bin to find the most likely set of N_i and reconstruct the mass function. The error bars in Figure 10 show the reconstructed mass function in four different redshift bins, while the solid histograms show the average density from the input mass function of Tinker et al. (2008). Figure 10 shows that we can well reconstruct the input mass function without assuming its functional form at the two lower-redshift bins. At higher redshift, the large weak-lensing noise makes the number of observed clusters limited even for a 5000 deg^2 mock sample, making it more challenging to perfectly recover the input mass function. Meanwhile, deviations from the lognormal distributions assumed for the mass bias at these redshift and mass bins might also contribute to the discrepancy found in Figure 10. Overall, however, we think that these reconstructions of mass function still give encouraging evidence that the mass bias derived in this work and the analytic selection function do give a good description of shear-selected cluster samples.

4. Applications

The importance of the mass bias reflects on statistical studies carried out with shear-selected cluster samples. Giles et al. (2015) have found the X-ray luminosity of shear-selected clusters to be lower compared to clusters with similar masses selected in X-ray (e.g., Mantz et al. 2010; Mahdavi et al. 2013). In this section we reanalyze their sample with the inclusion of the mass bias found in Section 3 to see whether such a discrepancy can be resolved. We emphasize that our goal here is not to carry out a complete analysis on the scaling relation but just to demonstrate the need for the mass bias in shear-selected cluster samples.

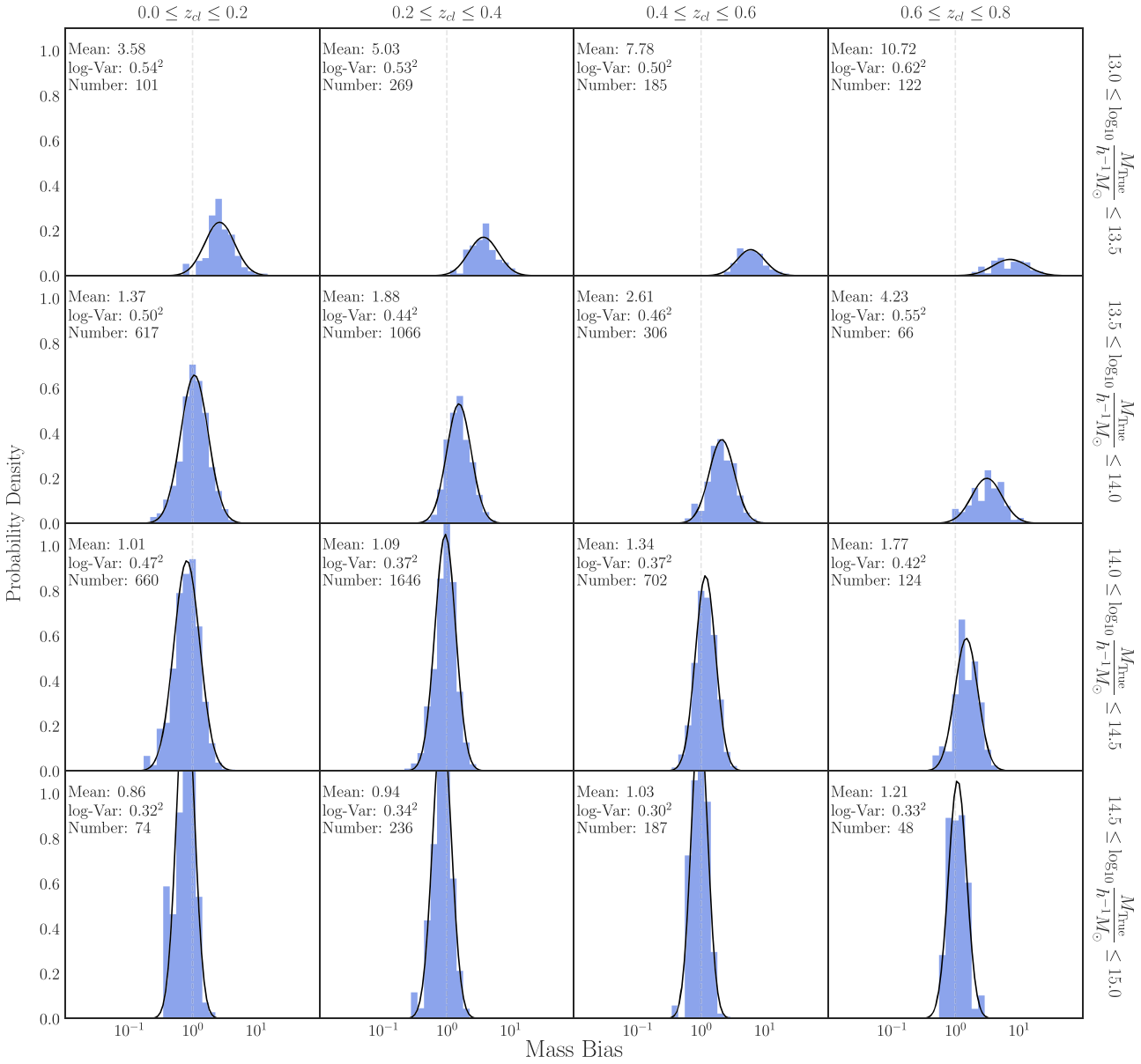

Figure 9. The histograms show the probability density function (pdf) of the mass bias (Equation (26)) in a 4×4 grid in redshift and mass. The mean of the distribution and the variance in logarithmic space are quoted in the upper left corner in each panel. In each panel, a lognormal pdf according to these two parameters is overplotted by a solid line to see how well the distribution is described by the lognormal form. These histograms are based on an $n_{\rm gal} = 30$ arcmin^{-2} sample selected with a $\nu_{\rm threshold} \geqslant 4.0$ cut. The uncertainty due to halo triaxiality is included.

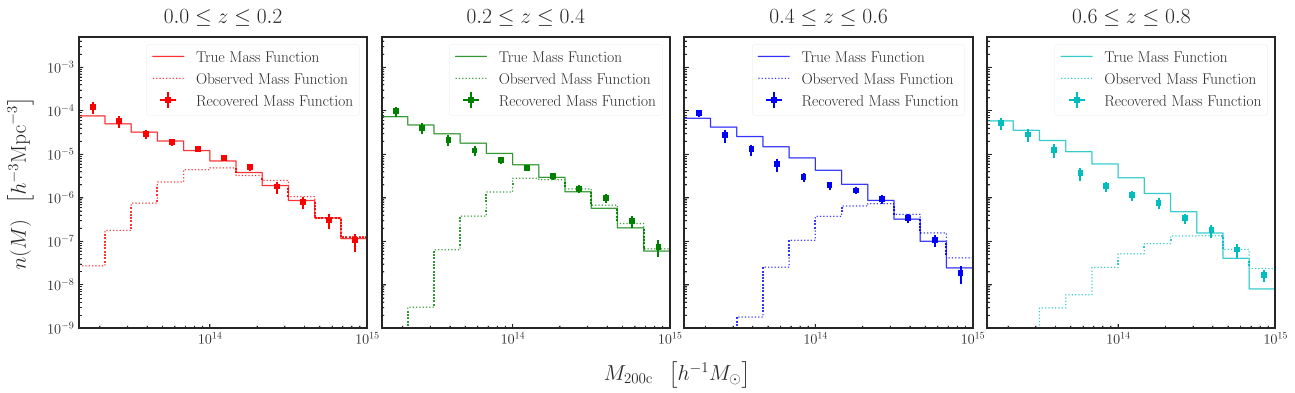

Figure 10. Reconstruction of input mass function from the observed number counts of shear-selected clusters selected in an $n_{\rm gal} = 30$ arcmin^{-2} sample with a $\nu_{\rm threshold} \geqslant 4.0$ cut. The dotted histograms show the observed number density of clusters in this sample, and the reconstructed mass functions are shown in error bars. The true number density in each bin based on the input mass function from Tinker et al. (2008) is plotted as the solid histogram.

Table 1
X-Ray and Weak-lensing Properties for the 10 Clusters Presented in Giles et al. (2015)

Cluster Name	$n_{\rm gal}$ (arcmin^{-2})	z_{cl}	$L_{\rm X}$ (10^{43} erg s^{-1})	$M_{\rm WL,500}$ ($10^{14}\,M_{\odot}$)
SL J0225.7–0312	46.0	0.1395	7.31 ± 0.19	$1.97^{+0.47}_{-0.47}$
SL J1000.7+0137	37.1	0.2166	4.04 ± 0.17	$2.39^{+0.46}_{-0.53}$
SL J1647.7+3455	26.4	0.2592	1.38 ± 0.12	$2.00^{+0.67}_{-0.79}$
SL J0850.5+4512	30.7	0.1935	0.78 ± 0.14	$1.09^{+0.39}_{-0.43}$
SL J1135.6+3009	29.3	0.2078	...	$2.49^{+0.50}_{-0.56}$
SL J1204.4–0351	23.4	0.2609	3.43 ± 0.35	$1.20^{+0.50}_{-0.60}$
SL J1335.7+3731	29.6	0.4070	3.10 ± 0.71	$2.79^{+0.90}_{-1.01}$
SL J1337.7+3800	29.6	0.1798	0.66 ± 0.13	$1.24^{+0.36}_{-0.39}$
SL J1602.8+4335	38.0	0.4155	12.7 ± 1.14	$2.66^{+0.69}_{-0.71}$
SL J1634.1+5639	28.4	0.2377	0.63 ± 0.22	$0.87^{+0.39}_{-0.49}$

Note. The $n_{\rm gal}$ column represents the average surface number density of source galaxies in the field where the cluster is observed. The z_{cl} column is the cluster spectroscopy redshift obtained in Hamana et al. (2009). L_X denotes core-excised bolometric X-ray luminosity, and $M_{\rm WL,500}$ denotes cluster mass M_{500c} derived with weak lensing.

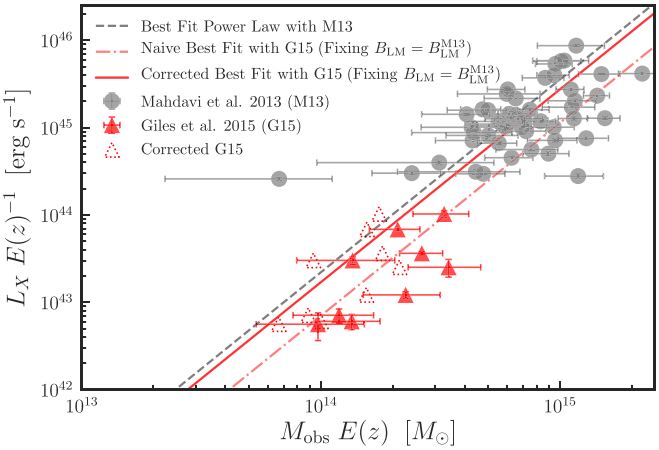

Figure 11. Analyses of the scaling relation between X-ray luminosity L_X and cluster masses $M_{\rm obs}$ from weak lensing on the data set from Mahdavi et al. (2013) (gray circles) and Giles et al. (2015) (filled red triangles). A direct power-law fit to the M13 sample is shown by the dashed black line. The best-fit slope $B_{LM}^{\rm M13}$ is fixed in the analyses on the G15 sample. The dashed–dotted red line shows the direct fit to the G15 sample, whereas the solid red line represents the corrected fit including the mass bias. The correction for each individual cluster in G15 is shown with open red triangles.

4.1. Cluster Samples

First, we briefly summarize the sample presented in Giles et al. (2015). The cluster candidates were selected as peaks on the 16.72 deg^2 mass map in the Subaru Weak-lensing survey (Miyazaki et al. 2007) with a $\nu_{\rm threshold} = 3.69$ cut. The survey targeted 16 different fields containing X-ray data. Since each field was observed under different seeing conditions, the resulting surface number density of galaxies around the cluster candidates was also different. This information is summarized in Table 1. A total of 28 of these candidates were spectroscopically confirmed in follow-up observations (Hamana et al. 2009), for which weak-lensing masses can therefore be derived. Giles et al. (2015) conducted X-ray studies on 10 of these clusters, in which eight of them obtained dedicated *Chandra* pointings and the remaining two were observed in the COSMOS field with *Chandra* and in the *XMM*–LSS field with *XMM*, respectively. The weak-lensing and X-ray properties of these 10 clusters are given in Table 1.

The X-ray luminosity and weak-lensing mass scaling relation (L_X–M relation) showed that the 10 shear-selected clusters were X-ray underluminous by a factor of ∼2–3 compared with X-ray-selected clusters presented in Mahdavi et al. (2013). A similar anomaly was also found when comparing with the X-ray samples in Mantz et al. (2010). Giles et al. (2015) have already presented rough estimates on the mass bias to correct the weak-lensing mass. The discrepancies were attributed to miscentering, selection bias, and the triaxial nature of halos. In this paper, we have presented a more rigorous and consistent treatment of these effects. In the following section, we will adopt our mass bias and examine its impact on the cluster scaling relation.

4.2. Reanalysis of $L_{\rm X}$–M Scaling Relation

Here we follow the procedure in Giles et al. (2015, hereafter G15) to analyze the L_X–M scaling relation taking account of the mass bias. The scaling relation is described by the following power law:

$$L_X E(z)^{-1} = L_0 \left\{ \frac{E(z) M_{\rm True}}{M_0} \right\}^{B_{LM}}, \tag{28}$$

where $E(z)$ is the dimensionless Hubble parameter and the parameters (L_0, B_{LM}) are to be determined from data. The pivot mass M_0 is taken to be $2 \times 10^{14}\,M_{\odot}$. The 10 shear-selected clusters alone cannot provide enough constraining power to fit (L_0, B_{LM}) simultaneously. We therefore rely on a larger sample of X-ray-selected clusters presented in Mahdavi et al. (2013, hereafter M13) to determine the slope B_{LM} first. The actual data presented here are taken from the erratum (Mahdavi et al. 2014). The cosmological parameters adopted in the two studies are exactly the same; hence, the two samples are compared directly. The best-fit parameters are derived using the orthogonal distance regression (Boggs & Rogers 1990) in order to properly take into account uncertainties on both variables. The data in M13 give $B_{LM}^{\rm M13} = 2.21 \pm 0.37$ and $L_0^{\rm M13} = (10.14 \pm 5.10) \times 10^{43}$ erg s^{-1}. Fixing $B_{LM} = B_{LM}^{\rm M13}$, the shear-selected sample gives $L_0^{\rm G15} = (3.23 \pm 0.77) \times 10^{43}$ erg s^{-1}, corresponding to a $\sim 1.4\sigma$ deviation from the X-ray sample. Figure 11 shows the fitting results obtained from the two samples. We find that our fitting result without the correction of the mass bias is consistent with G15.

The discrepancy between G15 and M13 should be to some extent ascribed to the mass bias in shear-selected clusters. As the mass bias depends sensitively on the cluster redshifts but varies little over $M_{\rm obs}$, we add the following relation when fitting the scaling relation:

$$M_{\rm True} = b(z_{cl}) M_{\rm obs}. \tag{29}$$

The weak-lensing masses $M_{\rm obs}$ for these 10 clusters were derived in Hamana et al. (2009) following a procedure similar to those described in Section 2.3. Therefore, here we calculate the bias as in Section 2 with a $\nu_{\rm threshold} = 3.69$ selection. The

average surface density of source galaxies around the 10 clusters is $\approx 30\,\mathrm{arcmin}^{-2}$. Additional scatter due to triaxiality is also included. Since it is customary to use the mass M_{500c} in X-ray studies, we recompute the mass bias changing the mass definition from M_{200c} to M_{500c} in Equation (26). We note that there are still two inconsistencies between our analyses in Section 2.3 and those in Hamana et al. (2009): the probability distribution of source galaxies and the cosmological parameters assumed when deriving the weak-lensing mass are different. Nevertheless, if we adopt $n_{\rm gal} = 30\,\mathrm{arcmin}^{-2}$, our numerical calculation shows that Equation (7) is almost identical to the functional form assumed in Hamana et al. (2009). The difference in cosmological parameters induces a deviation in angular diameter distance only by $\lesssim 1\%$ within a reasonable range of redshift. Moreover, the most significant effect from the above-mentioned deviations is in the calculation of $\Sigma_{\rm cri}$, which will be canceled out in the mass bias, as we are taking the ratio between masses. Therefore, the usage of our mass bias to this shear-selected cluster sample is justified.

We then follow the same procedure to refit the scaling relation to these 10 clusters. Since this sample was selected with a rather low S/N cut, according to our results the observed mass for each individual cluster needs to be corrected by a level ranging from -30% to -90%. The corrected mass for each of these clusters is shown with dotted open triangles in Figure 11. With a fixed slope of $B_{LM} = 2.21 \pm 0.37$, the reanalysis on the G15 data gives $L_0^{\rm G15,unbias} = (7.81 \pm 1.93) \times 10^{43}\,\mathrm{erg\,s^{-1}}$. The tension in the intercept is reduced to $\sim 0.5\sigma$ after our reanalysis. The result of the new fit is also shown in Figure 11.

We emphasize that our analysis here is far from rigorous. Modern analyses on the scaling relation should include effects such as the Eddington bias, the covariance between variables, and scattering in the mass bias (for a state-of-the-art example, see Dietrich et al. 2019). Although our analysis clearly demonstrated that the mass bias can definitely reduce the tension on the X-ray properties of shear-selected clusters, a more thorough analysis on cleaner and larger shear-selected samples such as those presented in Miyazaki et al. (2018) is needed to draw a definitive conclusion on this issue.

5. Conclusions

We have studied the bias on masses measured with weak lensing for shear-selected cluster samples, which are constructed from high-S/N peaks in weak-lensing mass maps. Since weak-lensing mass maps that are used to define shear-selected cluster samples and tangential shear profiles of individual clusters that are used to measure their masses share the same noise, including the statistical noise, the uncorrelated structure along the line of sight, and the effect of halo triaxiality, the mass bias on shear-selected cluster samples is expected to be significant. We have quantified this bias accurately using a hybrid approach where the density profile of individual halos is modeled with a simple NFW profile yet high-resolution ray-tracing simulations are used to model the noise originating from the line-of-sight structure. This approach allows us to construct large mock catalogs needed to derive the mass bias accurately.

We have found that the mass bias is indeed significant, particularly for shear-selected clusters constructed from the low number density of source galaxies or from the low S/N threshold of mass map peaks. We have investigated the dependence of the mass bias on different parameters, including true halo masses, cluster redshifts, and observed weak-lensing masses. We find that the mass bias depends sensitively on cluster redshifts such that clusters at higher redshifts have a larger mass bias. On the other hand, the mass bias depends modestly on observed weak-lensing masses. The halo triaxiality has a nonnegligible impact on the mass bias, especially when the S/N threshold or the source galaxy number density is high.

To demonstrate the impact of the mass bias on scaling relation studies, we have applied our result to a shear-selected cluster sample constructed by Giles et al. (2015). Although it has been claimed, based on analyses of the scaling relation between X-ray luminosity and mass, that shear-selected clusters appear X-ray underluminous by a factor of $\sim$2–3 compared with X-ray-selected clusters, our reanalysis taking proper account of the mass bias for shear-selected clusters has indicated that the discrepancy is significantly reduced. This highlights the importance of the mass bias for shear-selected cluster samples.

Even though the mass bias is large for shear-selected cluster samples, an important advantage of shear-selected cluster samples over other cluster samples is that we can accurately and robustly quantify the mean and scatter of the mass bias. This is because the ingredients needed for calculating the mass bias, including the density profile of clusters, the large-scale structure noise, and halo triaxiality, are fairly well known. In contrast, there are large uncertainties associated with cluster galaxy populations and the physical state of the ICM, which implies that it is difficult to robustly model selection functions for cluster samples constructed based on baryonic properties in clusters. One such example is the cool-core bias (Eckert et al. 2011), which modifies posterior distributions of cluster properties such as concentration parameters, asphericity, and the amount of substructures and hence may induce weak-lensing mass bias in a nontrivial way, even though the effect would be smaller than the one studied in this paper. Given the lack of full understanding of baryonic properties in clusters, we face the difficulty in converting these selection functions into the mass bias. Therefore, studies of scaling relations for shear-selected clusters, with the correction of the mass bias as done in this paper, will help identify and quantify known and unknown systematics inherent to scaling relations derived for optical, X-ray, and Sunyaev–Zel'dovich cluster samples. While the current limitation lies in the small number of shear-selected clusters available, the ongoing Subaru HSC survey, as well as future surveys such as Euclid (Laureijs et al. 2011) and Large Synoptic Survey Telescope (LSST Science Collaboration et al. 2009), can construct much larger samples of shear-selected clusters, which will be enormously useful for improving our understanding of cluster scaling relations and hence the reliability of cluster cosmology.

We thank an anonymous referee for valuable comments and suggestions. K.-F.C. and Y.-T.L. acknowledge support from the Ministry of Science and Technology grants MOST 105-2112-M-001-028-MY3 and MOST 108-2112-M-001-011 and an Academia Sinica Career Development Award (2017-2021). This work was supported in part by World Premier International Research Center Initiative (WPI Initiative), MEXT, Japan, and JSPS KAKENHI grant Nos. JP15H05892 and JP18K03693. Numerical calculations are performed through

the Python packages Numpy (Oliphant 2006) and Scipy (Virtanen et al. 2020). Many of the cosmological and astrophysical calculations in this work rely on the routines wrapped up in Colossus (Diemer 2018). Plots are made available thanks to matplotlib (Hunter 2007).

ORCID iDs

Kai-Feng Chen https://orcid.org/0000-0002-3839-0230
Masamune Oguri https://orcid.org/0000-0003-3484-399X
Yen-Ting Lin https://orcid.org/0000-0001-7146-4687
Satoshi Miyazaki https://orcid.org/0000-0002-1962-904X

References

Aihara, H., Arimoto, N., Armstrong, R., et al. 2018, PASJ, 70, S4
Allen, S. W., Evrard, A. E., & Mantz, A. B. 2011, ARA&A, 49, 409
Bahé, Y. M., McCarthy, I. G., & King, L. J. 2012, MNRAS, 421, 1073
Bardeau, S., Soucail, G., Kneib, J.-P., et al. 2007, A&A, 470, 449
Becker, M. R., & Kravtsov, A. V. 2011, ApJ, 740, 25
Bellagamba, F., Roncarelli, M., Maturi, M., & Moscardini, L. 2018, MNRAS, 473, 5221
Bleem, L. E., Stalder, B., de Haan, T., et al. 2015, ApJS, 216, 27
Bocquet, S., Dietrich, J. P., Schrabback, T., et al. 2019, ApJ, 878, 55
Boggs, P. T., & Rogers, J. E. 1990, in Statistical Analysis of Measurement Error Models and Applications, Contemporary Mathematics, Vol. 112, ed. P. J. Brown & W. A. Fuller (Providence, RI: American Mathematical Society), 183
Bullock, J. S., Kolatt, T. S., Sigad, Y., et al. 2001, MNRAS, 321, 559
Clerc, N., Adami, C., Lieu, M., et al. 2014, MNRAS, 444, 2723
Clowe, D., De Lucia, G., & King, L. 2004, MNRAS, 350, 1038
Corless, V. L., & King, L. J. 2007, MNRAS, 380, 149
de Haan, T., Benson, B. A., Bleem, L. E., et al. 2016, ApJ, 832, 95
Diemer, B. 2018, ApJS, 239, 35
Diemer, B., & Joyce, M. 2019, ApJ, 871, 168
Dietrich, J. P., Bocquet, S., Schrabback, T., et al. 2019, MNRAS, 483, 2871
Eckert, D., Molendi, S., & Paltani, S. 2011, A&A, 526, A79
Eddington, A. S. 1913, MNRAS, 73, 359
Edge, A. C., Stewart, G. C., Fabian, A. C., & Arnaud, K. A. 1990, MNRAS, 245, 559
Einasto, J. 1965, TrAlm, 5, 87
Foreman-Mackey, D., Hogg, D. W., Lang, D., & Goodman, J. 2013, PASP, 125, 306
Gao, L., Navarro, J. F., Cole, S., et al. 2008, MNRAS, 387, 536
Giles, P. A., Maughan, B. J., Hamana, T., et al. 2015, MNRAS, 447, 3044
Gioia, I. M., Henry, J. P., Maccacaro, T., et al. 1990, ApJL, 356, L35
Gladders, M. D., & Yee, H. K. C. 2005, ApJS, 157, 1
Goodman, J., & Weare, J. 2010, CAMCS, 5, 65
Graham, A. W., Merritt, D., Moore, B., Diemand, J., & Terzić, B. 2006, AJ, 132, 2701
Hamana, T., Miyazaki, S., Kashikawa, N., et al. 2009, PASJ, 61, 833
Hamana, T., Oguri, M., Shirasaki, M., & Sato, M. 2012, MNRAS, 425, 2287
Hasselfield, M., Hilton, M., Marriage, T. A., et al. 2013, JCAP, 7, 008
Hinshaw, G., Larson, D., Komatsu, E., et al. 2013, ApJS, 208, 19
Hoekstra, H. 2003, MNRAS, 339, 1155
Hoekstra, H. 2007, MNRAS, 379, 317
Hunter, J. D. 2007, CSE, 9, 90
Huterer, D., Kirkby, D., Bean, R., et al. 2015, APh, 63, 23
Jing, Y. P., & Suto, Y. 2002, ApJ, 574, 538
Koester, B. P., McKay, T. A., Annis, J., et al. 2007, ApJ, 660, 239
Laureijs, R., Amiaux, J., Arduini, S., et al. 2011, arXiv:1110.3193
LSST Science Collaboration, Abell, P. A., Allison, J., et al. 2009, arXiv:0912.0201
Ludlow, A. D., Bose, S., Angulo, R. E., et al. 2016, MNRAS, 460, 1214
Macciò, A. V., Dutton, A. A., & van den Bosch, F. C. 2008, MNRAS, 391, 1940
Mahdavi, A., Hoekstra, H., Babul, A., et al. 2013, ApJ, 767, 116
Mahdavi, A., Hoekstra, H., Babul, A., et al. 2014, ApJ, 794, 175
Majumdar, S., & Mohr, J. J. 2004, ApJ, 613, 41
Mantz, A., Allen, S. W., Rapetti, D., & Ebeling, H. 2010, MNRAS, 406, 1759
Mantz, A. B., Allen, S. W., Morris, R. G., et al. 2014, MNRAS, 440, 2077
Meneghetti, M., Rasia, E., Merten, J., et al. 2010, A&A, 514, A93
Merritt, D., Graham, A. W., Moore, B., Diemand, J., & Terzić, B. 2006, AJ, 132, 2685
Milkeraitis, M., van Waerbeke, L., Heymans, C., et al. 2010, MNRAS, 406, 673
Miyazaki, S., Hamana, T., Ellis, R. S., et al. 2007, ApJ, 669, 714
Miyazaki, S., Oguri, M., Hamana, T., et al. 2015, ApJ, 807, 22
Miyazaki, S., Oguri, M., Hamana, T., et al. 2018, PASJ, 70, S27
Navarro, J. F., Frenk, C. S., & White, S. D. M. 1997, ApJ, 490, 493
Navarro, J. F., Ludlow, A., Springel, V., et al. 2010, MNRAS, 402, 21
Oguri, M. 2014, MNRAS, 444, 147
Oguri, M., & Blandford, R. D. 2009, MNRAS, 392, 930
Oguri, M., & Hamana, T. 2011, MNRAS, 414, 1851
Oguri, M., Lin, Y.-T., Lin, S.-C., et al. 2018, PASJ, 70, S20
Oguri, M., & Takada, M. 2011, PhRvD, 83, 023008
Oguri, M., Takada, M., Umetsu, K., & Broadhurst, T. 2005, ApJ, 632, 841
Okabe, N., & Smith, G. P. 2016, MNRAS, 461, 3794
Okabe, N., Zhang, Y. Y., Finoguenov, A., et al. 2010, ApJ, 721, 875
Oliphant, T. 2006, NumPy: A Guide to NumPy (Spanish Fork, UT: Trelgol Publishing), http://www.numpy.org/
Planck Collaboration, Ade, P. A. R., Aghanim, N., et al. 2016, A&A, 594, A24
Prada, F., Klypin, A. A., Cuesta, A. J., Betancort-Rijo, J. E., & Primack, J. 2012, MNRAS, 423, 3018
Rozo, E., Wechsler, R. H., Rykoff, E. S., et al. 2010, ApJ, 708, 645
Rykoff, E. S., Rozo, E., Hollowood, D., et al. 2016, ApJS, 224, 1
Sato, M., Hamana, T., Takahashi, R., et al. 2009, ApJ, 701, 945
Schirmer, M., Erben, T., Hetterscheidt, M., & Schneider, P. 2007, A&A, 462, 875
Shan, H., Kneib, J.-P., Tao, C., et al. 2012, ApJ, 748, 56
Sunyaev, R. A., & Zeldovich, Y. B. 1972, CoASP, 4, 173
Szabo, T., Pierpaoli, E., Dong, F., Pipino, A., & Gunn, J. 2011, ApJ, 736, 21
Tinker, J., Kravtsov, A. V., Klypin, A., et al. 2008, ApJ, 688, 709
Umetsu, K., Zitrin, A., Gruen, D., et al. 2016, ApJ, 821, 116
van Waerbeke, L. 2000, MNRAS, 313, 524
Van Waerbeke, L., Mellier, Y., Radovich, M., et al. 2001, A&A, 374, 757
Vikhlinin, A., Kravtsov, A. V., Burenin, R. A., et al. 2009, ApJ, 692, 1060
Vikhlinin, A., McNamara, B. R., Forman, W., et al. 1998, ApJ, 502, 558
Virtanen, P., Gommers, R., Oliphant, T. E., et al. 2020, Nat. Methods, 17, 261
Warren, M. S., Quinn, P. J., Salmon, J. K., & Zurek, W. H. 1992, ApJ, 399, 405
Weinberg, D. H., Mortonson, M. J., Eisenstein, D. J., et al. 2013, PhR, 530, 87
Wen, Z. L., Han, J. L., & Liu, F. S. 2009, ApJS, 183, 197
Wittman, D., Tyson, J. A., Margoniner, V. E., Cohen, J. G., & Dell'Antonio, I. P. 2001, ApJL, 557, L89
Wright, C. O., & Brainerd, T. G. 2000, ApJ, 534, 34
Wu, H.-Y., Rozo, E., & Wechsler, R. H. 2010, ApJ, 713, 1207
Zhang, Y.-Y., Okabe, N., Finoguenov, A., et al. 2010, ApJ, 711, 1033